Surface topography analysis of ball end milled tool steel surfaces

Biondani, Francesco; Bissacco, Giuliano; Hansen, Hans Nørgaard

Published in:
Procedia CIRP

Link to article, DOI:
10.1016/j.procir.2020.03.002

Publication date:
2020

Document Version
Publisher's PDF, also known as Version of record

Available online at www.sciencedirect.com

ScienceDirect

Procedia CIRP 87 (2020) 153–158

www.elsevier.com/locate/procedia

5th CIRP CSI 2020

Surface topography analysis of ball end milled tool steel surfaces

Francesco Biondani[a]*, Giuliano Bissacco[a], Hans Nørgaard Hansen[a] *

[a]*Technical University of Denmark, Department of Mechanical Engineering, 2800 Kgs Lyngby, Denmark*

* Corresponding author. Tel.: +45 45254733; fax: +45 45251961. E-mail address: frgbio@mek.dtu.dk

Abstract

Many mechanical components require mirror–like surface appearance. When the application concerns the manufacturing of steel dies and moulds, material removal processes are the preferential choice in order to achieve the wanted dimensions and surface topography. In particular, ball milling is used in all those cases that require the machining of free form surfaces. When mirror-like surface appearance is in focus in such components, the final machining operations consists in a very shallow cut. The theoretical surface roughness (kinematic surface topography) that can be achieved in a finishing operation by ball end milling is orders of magnitude below the actual surface roughness. Beside runout and machine tool positioning errors, the quality of the cutting tools is a key factor in determining the surface topography. The combination of shallow depth of cut together with the finite size of the cutting edge radius of the tool are responsible for the occurrence of material smearing phenomena. Smearing, consisting in the accumulation of plastically deformed material over the surface, is particularly detrimental for the aesthetic functionality of machined components because it is responsible of the "foggy" appearance. In order to minimize the occurrence of the smeared material it is necessary to have a good understanding of the causes of the smearing formation process. The aim of this paper is the description and quantification of the smearing phenomena for ball end milling operations. The location of the smeared material is determined through SEM image analysis and related with the direction of the cutting speed and milling strategy. Subsequently the volume of the smeared material is quantified through a combination of confocal microscopy and SEM image analysis. Based on the volumetric analysis of the smeared material a new method for determining the Minimum Uncut Chip Thickness for the material is proposed.

Keywords: Smearing; Surface Topography; Minimu Uncut Chip Thickness

1. Introduction

Machining of steel moulds and dies, characterized by complex freefrom geometries, is performed by means of ball end mills. The surface topography of these components directly affects the surface appearance of the final machined products and therefore is of paramount importance.

The final surface topography is normally generated through finishing machining operations in which the surface quality is the main focus.

Small values of radial depth of cut and feed per tooth are used, resulting in small engagement angles and uncut chip thicknesses. This, in combination with a finite value of the cutting edge radius of the tool induces peculiar material deformation behavior related to the minimum uncut chip thickness phenomena [1].

The physical phenomena occurring at this last step determines the resulting surface topography and in turn the surface appearance of the component [2].

In this paper the surface topography resulting from the ball end milling process on tool steel is studied. Particular attention is given to the occurrence and location of the surface artifacts generated by plastic material deformation over the surface.

The volume of deformed (smeared) material is measured and the result is used to identify the minimum uncut chip thickness for the material. The outcome of this work can be used for improving the accuracy for models for surface generation prediction in ball end milling.

10.1016/j.procir.2020.03.002

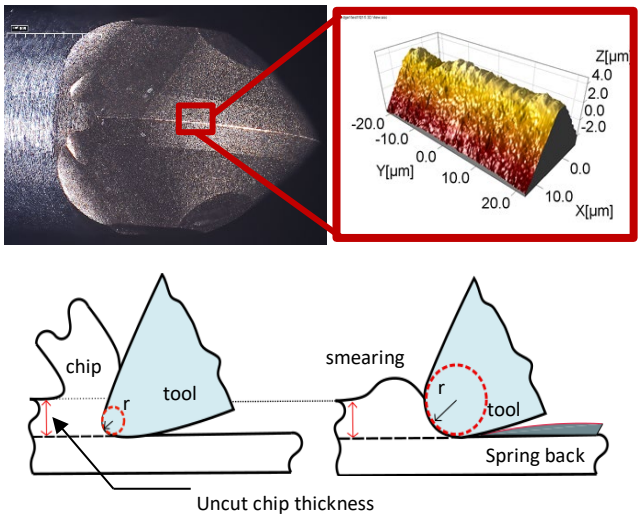

Fig. 1 Top: topography of a tool cutting edge measured with a confocal microscope. Bottom: smearing phenomena occurring when the MUCT condition is reached

2. Surface topography contributors

The topography of a machined surface is the result of the super position of several factors.

The overall enveloping geometry of the cutting tool, in combination with the tool path strategy, determines the shape and direction of the scallops and cusps remaining over the surface after machining [3].

In absence of chatter, straightness errors of the machine tool axis, tool deflection and tool runout influence the regularity of the scallops and alignment of the tool marks [4].

At the level of a single tooth mark, the micro geometry of the tool cutting edge plays a fundamental role [5].

At microscale, the cutting edge of a cutting tool is far from being perfectly smooth and sharp but shows a certain irregularity and a rounding radius that, at this length-scale, is not negligible (figure 1 top).

The edge irregularities are directly transferred on the workpiece surface as a result of the geometrical intersection between the tool and the workpiece.

On the other hand the edge rounding is responsible for all those phenomena depending on the minimum uncut chip thickness of the material, namely smearing and spring back and side flow.

2.1. Smearing and minimum uncut chip thickness

The minimum uncut chip thickness for a specific material, or shortly MUCT, can be defined as the minimum chip thickness under which material removal in stable cutting conditions is possible [6]. Cutting below the threshold of the MUCT leads to increased phenomena of plastic deformation and spring back: the chip is plastically smeared over the surface and, at the same time, increased elastic recovery of the machined surface takes place (figure 1 bottom).

Finishing milling, due to the uncut chip geometry, often operates in the region of plastic deformation below the threshold of the MUCT.

The value of the minimum uncut chip thickness for a given material is not constant but strictly related with the cutting edge radius of the tool.

For this reason, the ratio between the MUCT and the cutting edge radius, here called ρ, is more meaningful than the value of the MUCT itself: once the ratio ρ and the cutting edge radius are known, it is possible to derive the value of the MUCT.

Several research works have focused on the determinations of the MUCT for different materials. Experimental [7][8], analytical [9] and numerical [10] approaches have identified ρ for common materials used in micromilling applications such as carbon steel, copper, aluminum alloys, ranging from 0.05 to 0.4. However, for harder materials, such as tool steel commonly used in mould making applications, very few works can be found.

3. Experimental plan

In order to characterize the topography of ball end milled surfaces and develop a methodology for the identification of the ratio ρ by means of observation of the machined surface the following tests are carried out.

3.1. Machining plan

Four different milling strategies, illustrated in figure 2, are tested. Strategies A and B in figure 2a and 2b respectively, are characterized by zero tilt angle and non zero lead angle. Strategies C and D in figure 2c and 2d respectively, are characterized by non-zero tilt angle and zero lead angle.

Machining tests were performed using a cBN ball end mill with a diameter of 1 mm and zero helix angle. MQL lubrication was used. The relative inclination between the workpiece surface and the cutting tool was set to 40^0 by rotating the B axis of the machine tool table, thereby avoiding the region of zero cutting speed of the cutting tool. The cutting parameters used for the tests are listed in table 1

The workpiece consisted in a 20 x 20 mm bricks made of a commercial Cr-V-Mo tool steel (UNIMAX) with a hardness in the range of 54 HRC. All the machining operations were performed using a Mikron 400 ULP machine tool.

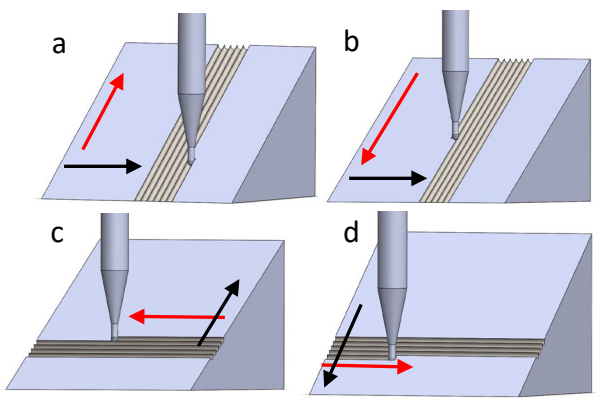

Fig. 2 Different machining strategies tested. The red arrows indicate the feed direction *fz*, the black ones the step over direction *ae*.

3.2. Surface characterization

The machined surfaces were observed using a SEM microscope Quanta FEG and a confocal microscope Olympus LEXT OLS4000 for quantifying the volume of the smeared material. For the confocal measurement a 100X magnification lens was used, with a field of view of 130 µm x 130 µm. The same confocal microscope was used to measure the cutting edge radius of the tool.

Table 1. Cutting parameters

Test	*Ap* /µm	*Ae* /µm	*Fz* /µm	*RPM*
#1 to # 5	15	50	15	13000
#6 to #8	15	50	20	13000

4. Surface texture analysis

4.1. Theoretical chip shape and chip orientation

In order to better understand the origins of the surface artifacts generated on the machined surface it is useful to have a clear idea of the theoretical chip shape, chip thickness distribution along the engagement and chip geometrical overlapping over the surface.

For this reason, a computer representations of the chip is built using Boolean operations between solid spheres and planes.

In this approximation, the surface machined by the tool in a previous pass is represented as a cylindrical surface. The unmachined surface is represented as a plane.

The cylindrical surface is intersected by two spherical surface, shifted by a quantity equal to the feed per tooth.

The intersecting volume enclosed between the two spherical surface, the cylindrical surface and the plane represents a good approximation of the theoretical chip shape.

Once a computer representations is established the local thickness of the chip can be calculated as it is showed as color map in figure 3.

It should be noticed that, with the cutting parameters combination described in this work, the majority of the surface

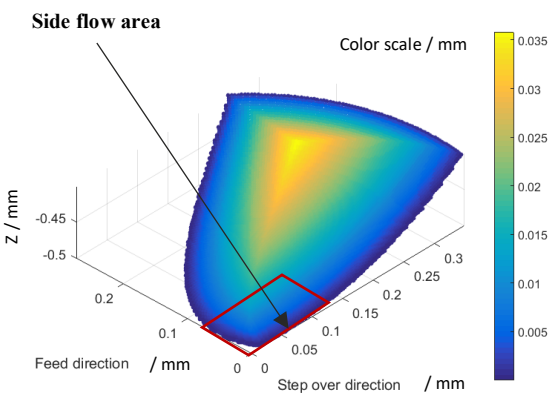

Fig. 3. Modelling of the local chip thickness. The colour scale is representative of the thickness. The red square encloses the area of the surface that will not be removed by subsequent tool passes

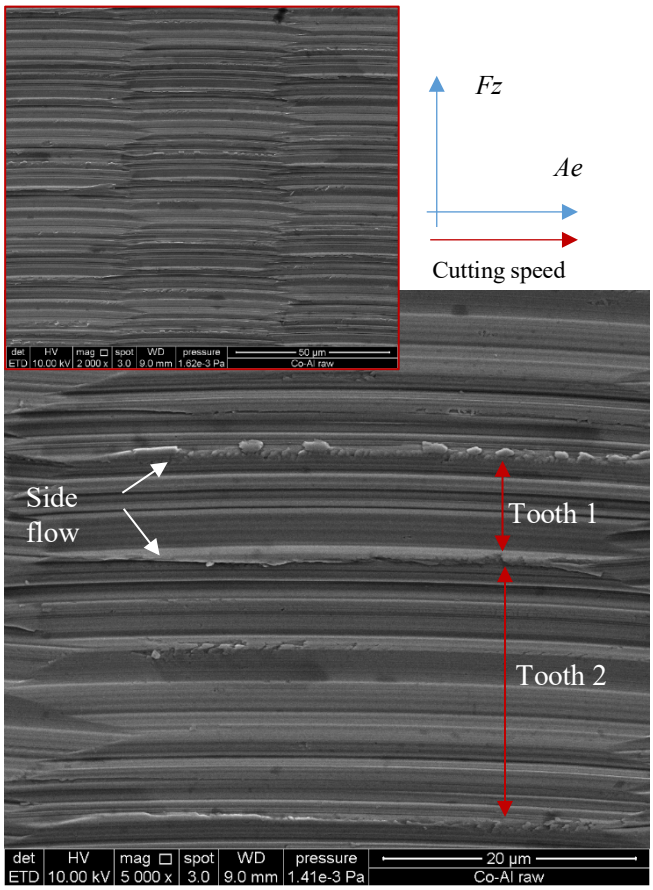

Fig. 4. SEM images of a surface machined with strategy A. The cutting parameters are indicated in table 1 for test #1.

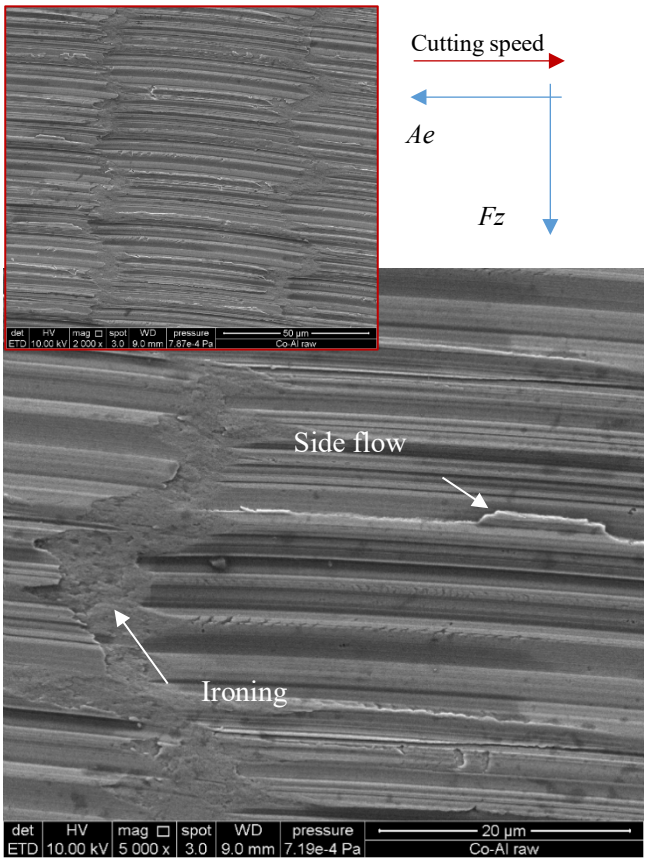

Fig. 5. SEM images of a surface machined with strategy B. The cutting parameters are indicated in table 1 for test#1.

generated in a single tooth engagement will be removed by the action of the subsequent tooth and by subsequent tool passes.

4.2. Strategy A and B: non zero lead angle

SEM images of the surface produced in strategy A are shown in figure 4 at various magnifications.

The feed direction, as well as the marks left by each single tooth of the cutting tool are clearly distinguishable.

Wave-like structures can be identified at the separation between two adjacent tooth marks. The generation of this structures can be associated to material side flow.

In fact, in this region of the surface, the cutting conditions are likely to enter the region below the MUCT.

Having the cutting configuration in mind, it is possible to determine the trajectory of each single tooth.

Referring to figure 4, the cutting action starts with the cutting edge entering from the left side and sweeping the material moving toward the right, in the direction of the yet to be machined surface. It can be noticed that the side flow occurs in the direction opposite to the tool feed and. orthogonal to the cutting speed (red arrow in the figure).

The high pressure applied by the cutting edge pushes the workpiece material to flow toward regions of lower pressure.

Because of the missing material, removed by the previous tooth, the workpiece material in this region is free to flow over the previously generated surface giving rise to the above mentioned wave like structures.

The magnitude of the wave structures is different between the tooth marks with one being more prominent than the other, furthermore the different distances between the structures indicate possible runout of the tool.

Figure 5 shows instead different magnifications of the surface generated in strategy B.

Many of the elements observed for the previous configuration are still evident: side flow, tooth marks and feed direction can clearly be identified.

However in this cutting configuration the cutting speed is directed toward the freshly generated surface. Referring figure 5, the tool cutting edge enters from the right side and exits on the left side. At the very end of the edge engagement the chip thickness is again approaching the MUCT conditions. The cutting edge cannot maintain a stable cut and the material is ironed until it tears, exhibiting a typical fracture surface appearance.

The comparison of the 3D topographies of the two surfaces measured with a confocal microscope can be seen in figure 6.

4.3. Strategy D and D: non zero tilt angle

The surface topographies generated by strategies C and D are shown in figure 7 and figure 8 respectively.

In comparison with cutting strategies A and B milling strategy, the teeth marks are not as evident on the SEM images.

Another distinguishing feature is the direction of the cutting speed that in those two cases results being parallel to the tool feed direction.

Due to the changing of the cutting speed direction, the location of side flow and material ironing change accordingly.

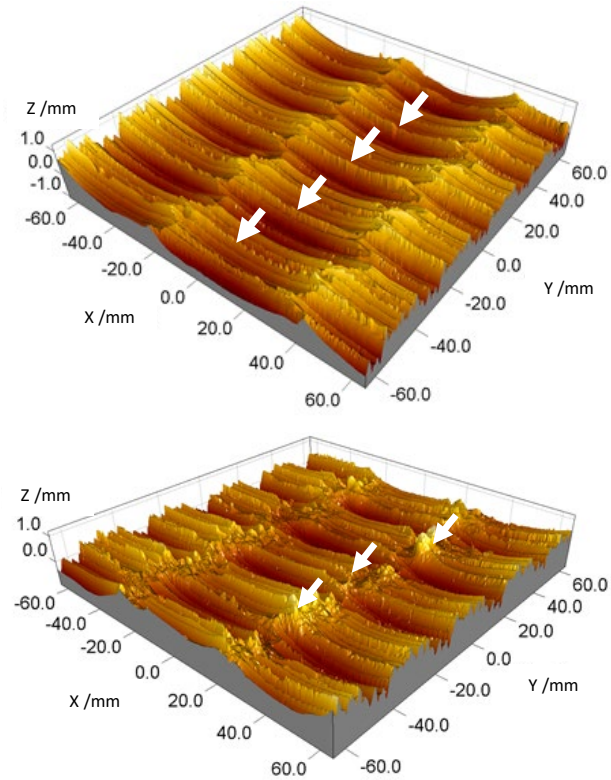

Fig. 6. Confocal images of a surface generated with strategy A (top) and B (bottom). The white arrows indicate areas where ironing (top) and side flow (bottom) take place.

Figure 7 shows the surface resulting from cutting strategy C. The side flow is located along the separation of adjacent tool tracks and flows in the direction of the surface machined in the previous tool pass.

Together with the side flow, also ironing phenomena are present, located between consecutive tooth marks. This is obvious if the cutting speed direction is again taken into consideration. In fact, the cutting edge exits the cut pushing the material toward the freshly machined surface opposite to the feed direction. As observed for the cutting strategies A and B this gives rise to material ironing. However, with cutting strategies C and D, no fracture-like structures are present but the deformed material overlaps the freshly generated surface.

Figure 8 shows the surface machined with strategy D. Side flow structures can be detected but, as the cutting speed points toward the surface to be machined, no ironing is present between tooth marks.

5. Determination of ρ

The knowledge of the local cutting edge radius of the tool, combined with the measurement of the smeared volume, allows the calculation, with some approximations, of the ratio ρ for the material. In Fact, the procedure described hereafter assumes that:

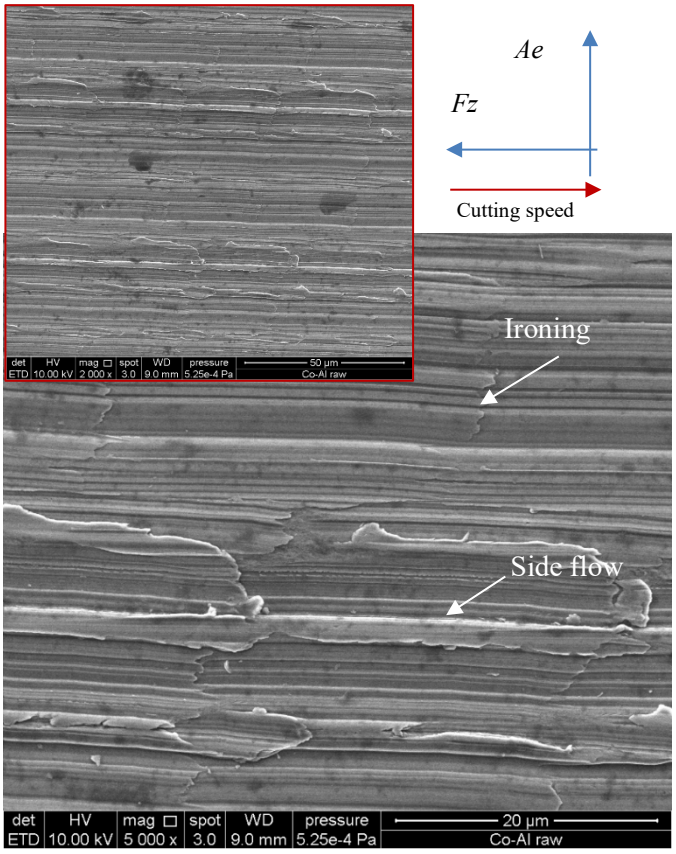

Fig. 7. SEM image of a surface machined with strategy C. The cutting parameters are the one indicated in table 1 for test#1.

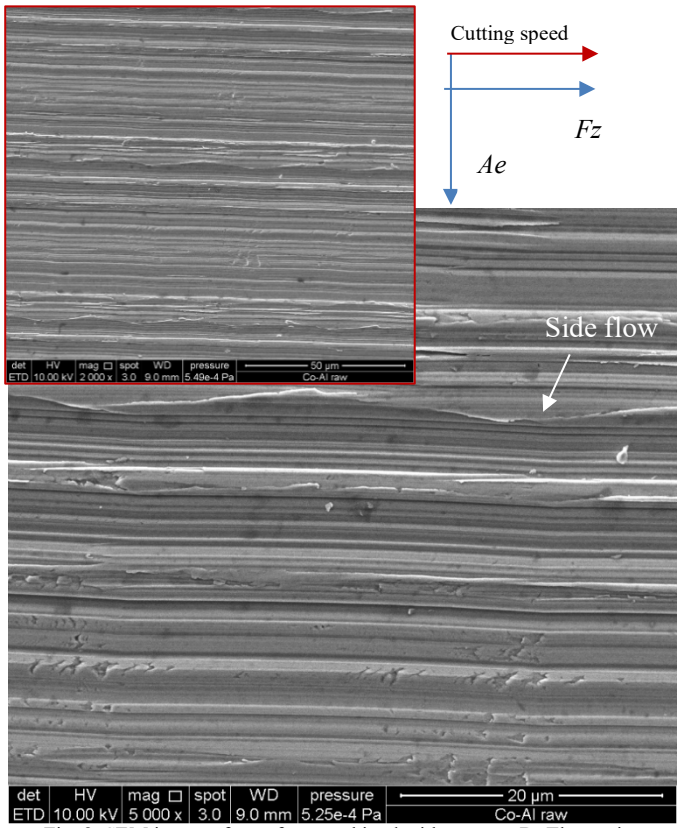

Fig. 8. SEM image of a surface machined with strategy D. The cutting parameters are the one indicated in table 1 for test#1.

- The theoretical chip shape is a good representation of the actual chip shape, neglecting imperfection on the cutter shape and machine tool errors on feed and step over position
- The tool is cutting in configuration A, where most of the smeared material produces side flow phenomena.

5.1. Measurement of the cutting edge radius

The measurement of the cutting edge of the tool was performed using images acquired with a confocal microscope using a 100x magnification objective lens.

The tool was tilted under the microscope using a specially designed fixture in such a way that the portion of the cutting edge engaging the material was centered in the field of view of the microscope.

From the confocal images, cross section profiles were extracted along the edge profile.

Edge measurements are heavily dependent on the fitting algorithm that is used to compute the edge radius. For this reason, a specially designed algorithm described by [11] was used in order to minimize the operator contribution to the edge radii calculation. The average edge radii (calculated using 20 different profiles) are shown in table 2 for the tools used in this work. The measurements are characterized by high standard deviation due to the irregularity of the cutting edge profile.

5.2. Measurement of smeared volume

The measurement of the smeared volumes is performed using a methodology involving comparison of SEM images and confocal microscopy images. The in depth description of the technique is discussed elsewhere [12], however a brief overview is given hereafter.

The 3D shape of the side flow is acquired by means of confocal microscopy. The measured surface is aligned with a SEM image of the same area in order to better resolve the boundary of the smearing structure. The exact location of the boundaries of the side flow are identified together with the highest point of the structures. Those points are used to compute the area of the cross section of the smeared volume, assuming a triangular cross section. The volume is then computed by multiplying the area by the extension of the smeared material. The computation is repeated for 8 different consecutive smearing structures. This methodology is applied for the calculation of the volumes for all the tests except for test 2. Test 2 represents the calculated volume resulting from Focus Ion Beam (FIB) cross sections of the smeared volume taken in the same location of test 1. In this latter case, the cross section is measured by counting the pixels of the FIB cross section on the SEM image, thereby eliminating the approximation of the triangular cross section. The volume is then computed as previously described. The value shown in table 2 is the result of the average of 6 different smearing structures. The purpose of test 2 is the verification of the proposed methodology for smeared volumes characterization. The difference between the two results is within their standard deviation interval. The results of this latter methodology for test 2 and the volume calculated in test 1 are compatible.

Table 2: Measured smeared volume Vsm and corriponding cutting edge radius (CE) that generated the volume. T#1 and T#2 represent measurements of the same volume with different methodologies.

TEST	*Vsm* /μm³	*Std* /μm³	*CE* /μm	*Std* /μm
1	26	10	4	1.5
2	35	16	4	1.5
3	27	7	4.4	1.6
4	34	1	4.5	1.6
5	36	4	4.5	1.6
6	22	2	4.8	1.7
7	16	2	4.9	1.8
8	17	4	5.1	1.9

5.3. Determination of MUCT

An estimation of the ratio ρ can be calculated once the smeared volume, local cutting edge radius of the tool and theoretical chip thickness are known.

By using the theoretical local chip thickness model described in 4.1, it is possible to selectively account for only the portion of the chip which local thickness falls below a threshold level (the minimum uncut chip thickness).

By integrating the local chip thickness values over this region it is possible to compute the theoretical chip volume below the minimum uncut chip thickness.

This operations can be repeated for a number of different MUCT values and the volume can be computed until a match between the theoretical smeared volume and the experimental measurement is found.

The matching value represents the MUCT for the material and the ratio between the minimum uncut chip thickness and the measured cutting edge radius is the value of the coefficient *ρ*. In the chart in figure 9 the resulting ratio *ρ* is shown. The ratio is calculated taking into account the standard deviation 1 sigma for the measurement of the cutting edge and for the measurement of the volume. The standard deviation of the measurements is representative of their repeatability. Due to the lack of a measurement standard for volume and cutting edge radius it was not possible to draft a more accurate uncertainty budget. This results in a certain spread of the value of the ratio represented by the error bars. The different colors represent two different test conditions in which the feed per tooth was varied from 15 to 20 μm.

The calculated ratio *ρ* suggests that the minimum uncut chip thickness for the considered material is approximately 5% of the cutting edge radius of the tool.

6. Conclusions

In this work the topography of ball end milled surfaces was described. The machining strategy was found to be responsible for the location of smearing phenomena over the surface. In particular, the direction of the cutting speed influences the location of the material side flow that always occurs perpendicular to it. Ironing phenomena are again related with the cutting speed direction as they are observed whenever the cutting speed pushes the material toward the already machined surface. A new methodology for quantifying the ratio *ρ* edge

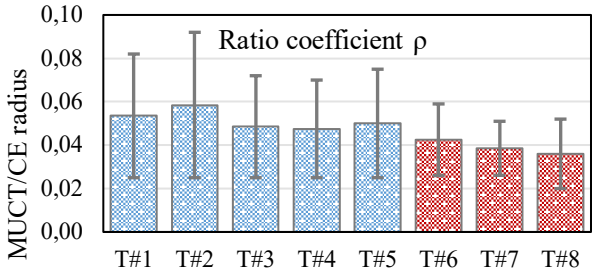

Fig. 9. Calculated ratio *ρ*: the blue colums represent test T#1 to T#5 where fz = 15/μm/tooth was used. The red colums represent test T#6 to T#7 where fz = 20 mm/tooth was used

was proposed. The methodology was tested with tool steel with 54 HRC suggesting a critical ratio of 0.05. The results of this work can be used to accurately model the surface generation process including smearing phenomena.

References

[1] G. Bissacco, H. N. Hansen, and J. Slunsky, "Modelling the cutting edge radius size effect for force prediction in micro milling," *CIRP Ann. - Manuf. Technol.*, vol. 57, pp. 113–116, 2008.

[2] F. G. Biondani, G. Bissacco, L. Pilný, H. N. Hansen, "Analysis and characterization of machined surfaces with aesthetic functionality," *Int. J. Autom. Technol.*, vol. 13, no. 2, pp. 261–269, 2019.

[3] M. F. Batista, A. R. Rodrigues, and R. T. Coelho, "Modelling and characterisation of roughness of moulds produced by high-speed machining with ball-nose end mill," *Proc. Inst. Mech. Eng. Part B J. Eng. Manuf.*, vol. 231, no. 6, pp. 933–944, 2017.

[4] L. Bo, C. Yanlong, C. Wenhua, and P. Jun, "Geometry simulation and evaluation of the surface topography in five-axis ball-end milling," *Int. J. Adv. Manuf. Technol.*, vol. 93, no. 5–8, pp. 1651–1667, 2017.

[5] F. G. Biondani and G. Bissacco, "Effect of cutting edge micro geometry on surface generation in ball end milling," *CIRP Ann.*, vol. 68, no. 1, pp. 571–574, 2019.

[6] B. Bergmann, B. Denkena, T. Grove, and T. Picker, "Chip Formation of Rounded Cutting Edges," *Int. J. Precis. Eng. Manuf.*, vol. 20, no. 1, pp. 37–44, 2019.

[7] H. Rezaei, M. H. Sadeghi, and E. Budak, "Determination of minimum uncut chip thickness under various machining conditions during micro-milling of Ti-6Al-4V," *Int. J. Adv. Manuf. Technol.*, vol. 95, no. 5–8, pp. 1617–1634, 2018.

[8] F. B. B. De Oliveira, A. R. Rodrigues, R. T. Coelho, and A. F. De Souza, "Size effect and minimum chip thickness in micromilling," *Int. J. Mach. Tools Manuf.*, vol. 89, no. February, pp. 39–54, Feb. 2015.

[9] X. Liu, R. E. DeVor, and S. G. Kapoor, "An Analytical Model for the Prediction of Minimum Chip Thickness in Micromachining," *J. Manuf. Sci. Eng.*, vol. 128, no. 2, p. 474, 2006.

[10] W. Chen, D. Huo, X. Teng, and Y. Sun, "Surface Generation Modelling for Micro end Milling Considering the Minimum Chip Thickness and Tool Runout," *Procedia CIRP*, vol. 58, pp. 364–369, 2017.

[11] C. F. Wyen, W. Knapp, and K. Wegener, "A new method for the characterisation of rounded cutting edges," *Int. J. Adv. Manuf. Technol.*, vol. 59, pp. 899–914, 2012.

[12] F. G. Biondani, G. Bissacco, and H. N. Hansen, "Methodologies for characterization of smearing micro geometry on ball end milled tool steel surfaces," in *World Congress on Micro and Nano Manufacturing WCMNM2018*, 2018, pp. 245–248.